RSC Advances

PAPER

View Article Online
View Journal | View Issue



Cite this: *RSC Adv.*, 2016, **6**, 47164

# Purification method dependent fluorescence from nitrogen-vacancy (NV) centers of nano-diamonds†

Ravi Kumar,[a] S. J. Yoon,[b] K. G. Lee,[b] Prabir Pal,[a] R. P. Pant,[a] C. K. Suman,[a] S. R. Dhakate,[a] Raj Kumar,[c] Devesh K. Avasthi[cd] and Dilip K. Singh*[a]

Received 18th January 2016
Accepted 29th April 2016

DOI: 10.1039/c6ra01510g

www.rsc.org/advances

Fluorescent nanodiamonds (FNDs) with high photo stability at a subwavelength scale are highly desirable for nano-photonics and bio-imaging applications. Nanodiamonds (NDs) with embedded fluorescent color centers made by ion-implantation need to be purified to remove the $sp^2$ layer on their surfaces which significantly degrades the optical properties. In this work, we discuss the structural and photo physical properties of NDs containing nitrogen-vacancy (NV) centers prepared by two different purification methods; chemical etching ($H_2SO_4$:$HNO_3$) and air oxidation (450 °C). Chemically etched NDs show better uniformity in their shape, de-aggregation and higher dispersibility in water as compared to air oxidized ones. On the other hand it is observed that air oxidation is more effective in removing the $sp^2$ layer and allows a higher fluorescence photon flux. Therefore, we suggest that air oxidation is more appropriate for bright fluorescent sources, and chemical etching is more appropriate for fluorescent markers in bio-imaging applications with high uniformity in shape and good dispersibility.

## Introduction

Fluorescent nanoparticles with a high quantum efficiency, high saturation photon flux, and a long photo stability with no photoemission intermittency are highly desirable for bio-photonic applications.[1] The search for such efficient fluorescent nanoparticles has been further pushed in the field of super-resolution optical imaging techniques like stimulated emission depletion microscopy (STED),[2,3] Stochastic optical resolution microscopy (STROM) and photo-activated localization microscopy (PALM) *etc.*[4,5] It is required that the emission from the nanoparticles should not overlap with auto-fluorescence from cells.[6] Organic dyes show limited photo-stability and emission rates and they are cytotoxic to cells.[7,8] Semiconductor quantum dots are considered as a suitable alternative to dyes in comparison, but they show photo-blinking and a high toxicity to cells limiting their wide use for optical imaging.[9–11] Various carbon nanostructures, like carbon nanotubes, fullerenes and strongly green luminescent graphene quantum dots, have been experimentally explored for this purpose,[12,13] however, they were later found to be cytotoxic.[14,15]

NDs are chemically inert, show least cytotoxicity and are biocompatible.[16–19] The nitrogen vacancy centers ($NV^-$ and $NV^0$) are the point defect centres consisting of a nitrogen atom at regular substitutional site and an adjacent lattice vacancy in regular diamond matrix. NV centres exhibits strong absorption near 532 nm and broad emission peak at ~700 nm. $NV^-$ centres have high quantum yield ($\phi \sim 1$),[20] high absorption cross section ($5 \times 10^{-17}$ $cm^2$) and no photo-bleaching.[21,22] Due to high Debye temperature of diamond and large energy band gap (5.5 eV); phonon interactions with NV centres are negligible.[23] Hence; NV centres behave as single atom like emission centres and shows this quantum mechanical behaviour up to the room temperature. FNDs show fluorescence resonance energy transfer (FRET) efficiency of about ~30%.[24] FNDs of size 4–100 nm has potential to be utilized as platform to incorporate multiple functionalities into single particle including payload of imaging probes or, anticancer drug molecule or, both. But, in the infrared region, the NV centre has 5 times lower brightness than usual fluorophores such as IRDye-800CW, which can be compensated by creating multiple color centers.

NDs have been synthesized by several methods: high pressure high temperature (HPHT) growth, detonation of hydrocarbons, pulsed laser deposition and using different CVD techniques.[25–29] Large abundance of nitrogen and lower energy requirements leads to their addition in the diamond structure during growth.[25] Entropy dictated disorderness allows a small concentration of substitutional vacant sites during growth.[30] These vacancies migrate at high temperature and are trapped by substitutional nitrogen atoms to form NV center. It has been intensively explored to experimentally increase the density of the vacancy and the resulting NV centers.

[a]*CSIR-National Physical Laboratory, New Delhi-110012, India. E-mail: dilip@mail.nplindia.org*

[b]*Department of Physics, Hanyang University, Seoul-133-791, Republic of Korea*

[c]*Inter University Accelerator Centre, Aruna Asaf Ali Marg, New Delhi-110067, India*

[d]*Amity Institute of Nanotechnology, Amity University, Noida-201313, India*

† Electronic supplementary information (ESI) available. See DOI: 10.1039/c6ra01510g

Non-diamond carbon phases present at the surface of NDs are detrimental to the fluorescence efficiency. It is important to remove non-diamond layers to obtain high quality FNDs. Previous reports show that different purification method adopted to oxidize the outer surface for purification of non-diamond carbon impurities forms different oxygen and nitrogen related functional groups to variety of extent.[26,31,32] The effect of different functional groups on the fluorescence of NDs is still an open question.[33] In this work, we study the structural, chemical, and photo physical properties of NV centers in NDs prepared by two purification methods: chemical etching and air oxidation. Such information is highly required to check the suitability of NV centers embedding NDs for bio-imaging and other nano photonic applications.

## Experimental details

### Raw materials, chemicals and milling materials and methods

Commercially procured HPHT grown micro-diamonds (element six, MICRON + MDA M0.10) were milled using high energy planetary ball mill (Insmart system, model no. PBM07) using steel balls of 10 mm diameter at 250 rpm. All the following milling processes were carried out in the intervals of one hour with 30 minutes break in between. The procured initial sample is referred as ND0. Initially, ND0 was dry milled for 9 hours (referred as ND9) and subsequently wet milled with water for 11 hours (referred as ND20). Further, resulting slurry was milled with NaCl (1 : 7 weight ratio) for additional 15 hours (referred as ND35). NaCl crystals assist in efficient mechanical energy transfer to the diamond particles. Post milling NaCl was removed from ND35 slurry by repeated rinsing with water and centrifugation. The graphitic and amorphous carbon present in the sample was purified by two different oxidation methods: (I) through acid reflux and (II) by air oxidation.

### Method-I: purification by acid reflux

In method-I, ND35 slurry was refluxed with conc. $H_2SO_4$ and conc. $HNO_3$ (3 : 1 v/v ratio) at 80 °C for 8 hours. Subsequently, it was five times rinsed with double distilled water and centrifuged. Obtained sample was dried in oven for 24 hours at 60 °C. Sample appeared brownish due to iron contamination from the steel vessel and the balls used for milling. Dried sample were crushed with mortar-pestle and were treated with conc. HCl for 4 hours to remove iron particles. HCl treatment leads effective etching of iron and results into de-aggregation of NDs by breakage of inter-particle covalent bonding by Fe(II) ions (C–Fe–C). HCl treated sample was diluted with water and centrifuged five times to remove acid content. After each dilution and centrifugation, the one third of solution was kept. Finally, it was oven dried. As purified sample has been referred as "ND35-R8HCL". The yield of method-I was 57.1 wt%.

### Method-II: purification by air oxidation

In method-II, ND-35 slurry was oxidized under ambient air flow at 450 °C using rapid thermal annealing at (50 °C $min^{-1}$) for 6 hours to remove inter particle graphitic and amorphous carbon layers. Air oxidation etches the non-diamond carbon from the inter-particle sites and outer surface of agglomerates with the addition of oxygen containing functional groups. On air oxidation, iron gets exposed on the outer surface, resulting into apparent reddish color. To remove iron impurities, it was treated with HCl for 4 hours and 5 times washed with water, centrifuged and was oven dried at 60 °C. This sample is referred as "ND35-OXDHCL". Method-II gives yield of 58.9 wt%.

### NV-center creation by ion-irradiation

Initial sample (ND0) and purified samples (ND35-R8HCL and ND35-OXDHCL) were ion-irradiated with $He^+$ ion beams for engineering of NV color centers at Inter-University Accelerator Center, New Delhi using custom made IUAC 50 keV accelerator (energy 35 keV, fluence $2 \times 10^{13}$ ions per $cm^2$, vacuum $10^{-6}$ Torr). Irradiated samples were annealed at 700 °C for 2 hours at rotary vacuum level.

### Characterization

The particle size and shape of the samples were characterized using scanning electron microscope (SEM) (model no. VP-EVO, MA-10, Carl-Zeiss, UK), transmission electron microscope (TEM) (model no. FEI, Tecnai T30). Raman and fluorescence spectra of the samples were recorded using 514 nm excitation from $Ar^+$ ion-laser and single monochromator equipped micro-Raman spectrometer with 50× objective lens using commercial system (Renishaw *in Via* Raman Microscope) in the backscattering geometry. Particle size analysis was carried out using blue wave laser diffraction analyzer based on Mie scattering (model no. Bluewave particle analyzer). X-ray diffraction pattern (XRD) was recorded using Rigaku made powder X-ray diffractometer (model-XRG 2 kW) at a scanning rate of 0.02 degree per s in the $2\theta$ range from 20° to 70° operating at 40 kV, 30 mA with automatic divergence slit using Cu-$K_\alpha$ radiation ($\lambda$ = 1.54059 Å). Thermo-gravimetric measurements were carried out at a heating rate of 5 °C $min^{-1}$ with 40 sccm $min^{-1}$ of air flow (using Mettler-Toledo TGA star system). The X-ray photo-electron spectroscopy (XPS) measurements were performed by using an Omicron μ-metal ultrahigh vacuum (UHV) system equipped with a monochromatic Al $K_\alpha$ X-ray source ($h\nu$ = 1486.6 eV) and a multi-channeltron hemispherical electron energy analyzer (EA 125). The samples were mounted on the sample plates using spot welded gold foils. An electrical contact was established between the sample surface and Omicron sample plate with a highly conducting UHV compatible silver (Ag) paint in order to avoid charging during the photoemission measurements due to their insulating nature of the samples. The samples were heated *in situ* at 300 °C under ultra-high vacuum conditions and then cooled down to room temperature before photoemission measurements. This heating procedure helped us to clean the sample surface as confirmed by the absence of surface adsorbed feature around ~532 eV in the O 1s core level spectra. The photoemission measurements were performed inside the analysis chamber under a base vacuum of $\sim 5.0 \times 10^{-11}$ mbar at room temperature. The binding energy of all the spectra was calibrated by considering Au $4f_{7/2}$ at 84.0 eV and the Fermi

energy ($E_F$) from Au foil in electrical contact with the sample. The energy resolution was 400 meV in case of XPS spectra using monochromatic Al $K_\alpha$ source. We have subtracted the background intensity due to secondary electrons from all the core level spectra using the Shirley and Tougaard background corrections.

## Results and discussion

Scanning electron microscope (SEM) images of initial sample (ND0), 35 hours milled sample (ND35) and purified samples ND35-R8HCL (through chemical etching, method-I) and ND35-OXDHCL (through air oxidation, method-II) are shown in Fig. S1 (ESI†). The average particle sizes were estimated using ImageJ software over more than 40 particles seen in the micrograph and are enlisted with standard deviation in Table 1.[34] ND0 shows the average particle size of 127.9 ± 67.9 nm, Fig. S1(a).† ND35 shows average particle size of 100.4 nm with calculated standard deviation of 27.0 nm, Fig. S1(b).† ND35-R8HCL shows average particle size of 91.7 ± 31.5 nm (Fig. S1(c)†), while ND35-OXDHCL shows average particle size of 128.8 ± 35.9 nm (Fig. S1(d)†). Fig. 1 shows the HRTEM micrographs of (a) ND0, (b) ND35, (c) ND35-R8HCl and (d) ND35-OXDHCL. The inset of the figures shows selected area electron diffraction (SAED) pattern taken on individual particle. For the analysis of the images and diffraction pattern ImageJ software was used. Fig. 1(a) shows initial particles were obloidal in nature (length 134.5 nm, width 65.5 nm). Milling for 35 hours (ND35) results into shape change from obloidal to mixture of rectangles and triangles (Fig. 1(b)). Milled sample also contained particles of very small size (~10 nm). The average length of the rectangle observed was 36.1 nm and width of 25.8 nm. ND35-R8HCL shows rectangular particles (length 70.5 nm, width 40.8 nm) along with very few triangular structures, Fig. 1(c). While ND35-OXDHCL shows rectangular particles (length 104.1 nm, width 62.6 nm) along with a significant numbers of irregular shaped particles Fig. 1(d). ND35-OXDHCL shows relatively higher agglomeration than the ND35-R8HCL. SAED pattern shows narrow ring like structure along with presence of sharp diffraction spots sitting over the rings. The estimated *d*-spacing along with corresponding lattice planes are indicated in insets. ND0 shows sharp spots sitting over a broad diffuse ring, indicating crystalline phase with a small fraction of amorphous carbon present as impurity. ND-35 shows multiple sharp rings with sharp spots sitting over them. Multiple ring structure originates from the impurities impregnated during milling as indicated by additional diffraction rings corresponding to Fe and NaCl. The initial sample shows diffraction rings with *d*-spacing 0.113 nm (220), 0.063 nm (400) and 0.052 nm (unidentified plane) of diamond. The assignment of lattice plane to the experimentally observed *d*-spacing has been done with reference to PCPDF data base # 060675. As per the PCPDF data base # 060675, the diamond shows diffraction spots corresponding to *d*-spacing of 0.206 nm (111), 0.126 nm (220), 0.107 nm (311), 0.089 nm (400), 0.082 nm (unassigned) respectively. The experimentally observed *d*-spacing from SAED pattern shows lower *d*-spacing than as expected from standard PCPDF database. This indicates initial nanoparticles ND-0 contain compressive lattice strain. Compressive strain relaxes after milling as indicated by change in the *d*-spacing from 0.113 nm to 0.136 nm for (220) plane, 0.063 nm to 0.066 nm for (400) plane. The SAED pattern of purified samples shows that acid refluxed NDs contains higher strain than the sample purified through air oxidation. The observed difference in the shape of the NDs purified through two methods in TEM arises due to difference in the amount of strain involved.

Fig. 2 shows the powder X-ray diffraction (XRD) pattern of sample milled for different periods and after purification. ND0 shows diffraction peak at ~43.8° (111) and 75.2° (220). Experimentally observed diffraction peaks are fitted with Voigt line shape. The change in the line profile parameters along with estimated crystallite size using Debye–Scherrer equation are summarized in Table S1 (ESI†). Fitting of (111) peak requires a weaker shoulder on lower Bragg angle 43.703° (crystallite size ~ 16.3 nm) in addition to 43.888° peak (crystallite size ~ 25.5 nm). With increasing milling period, the oscillating shift in (111) peak position indicates periodic creation and relaxation of compressive strain respectively from mechanical impacts.[35] Variation in the strain leads to varying disorders in the particles as reflected in terms of width (FWHM) change with increasing milling hours. No significant change in the crystallite size was observed upon dry milling for 09 hours. Additional wet milling for 11 hours shows reduction in the crystalline disorderness in terms of significant decrease in FWHM of (111) peak, but not any significant change in crystallite size. XRD measurements reveals that even prolonged milling, with different milling

Table 1 Particle size analysis

| | Particle size (nm) | | | | Crystallite size (nm) |
|---|---|---|---|---|---|
| | HRTEM | | | | |
| Sample | Length | Width | SEM | DLS | XRD |
| ND0 | 134.5 | 65.5 | 127.9 ± 67.9 | 160.0 | 16.3 and 25.6 |
| ND35 | 36.1 | 25.8 | 100.4 ± 27.0 | 80.0, 200.0, 350.0 | 23.2 |
| ND35-R8HCL | 70.5 | 40.8 | 91.7 ± 31.5 | 120.0 | 18.7 and 25.8 |
| ND35-OXDHCL | 104.1 | 62.6 | 128.8 ± 35.9 | 120.0 | 18.8 and 27.4 |

 

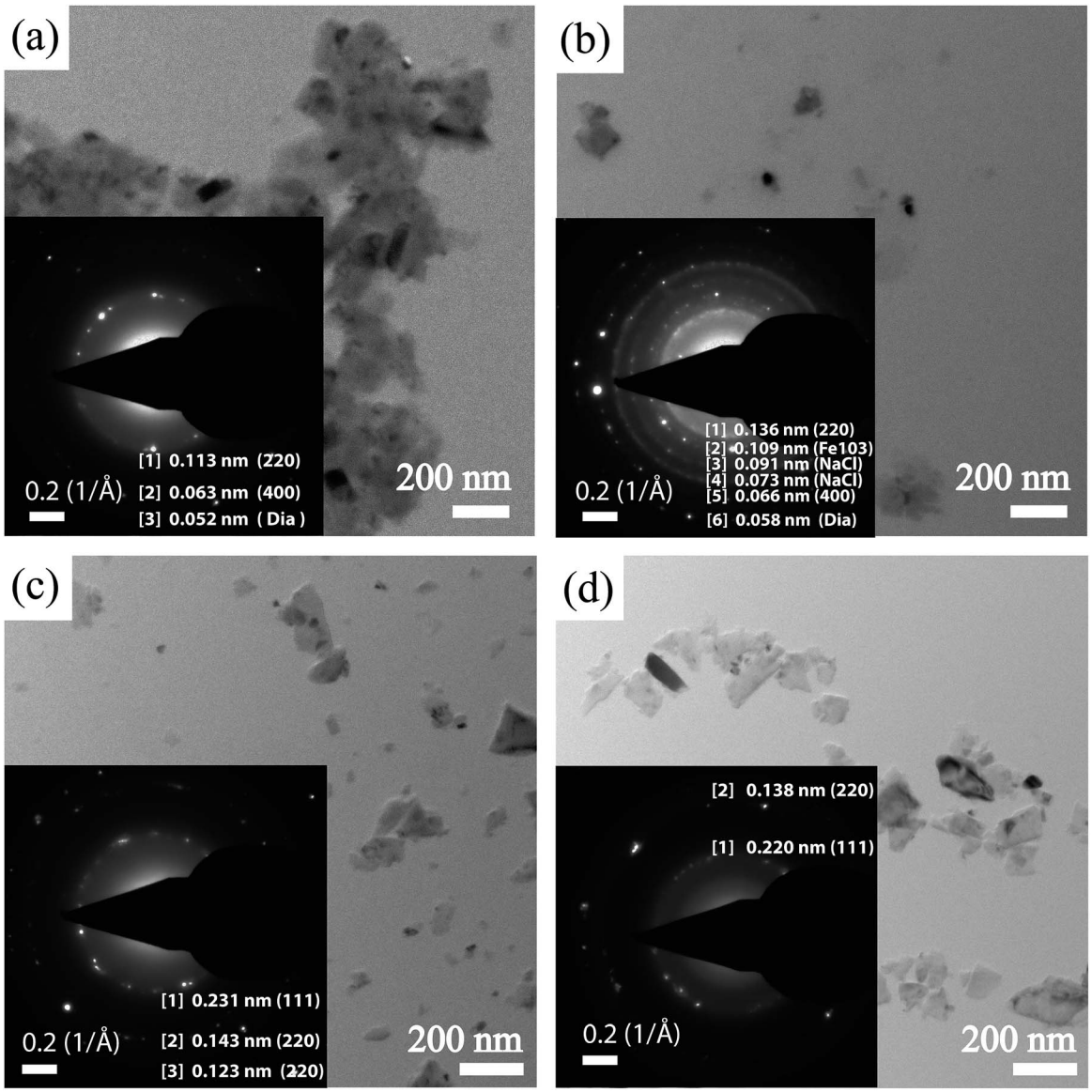


Fig. 1 Shows the TEM (SAED pattern in inset) of (a) initial sample, (b) milled sample ND35, (c) acid refluxed NDs: ND35-R8HCL and (d) air oxidized NDs: ND35-OXDHCL. Corresponding to the observed *d*-spacing in the SAED pattern, lattice planes are marked.

media (NaCl/water), the final change in the crystallite size remains minimal. Although from DLS measurements, we observe that the particle size decreases significantly within only 09 hours of milling, Fig. S2 (ESI†). This indicates that the primary particle size can be reduced only up to prevailing crystallite size and not below it. To reduce the particle size further, mechanical energy must be supplied at nanoscale with zirconium milling (bead assisted sonication disintegration), but large amorphitization of diamond phase and highly chemical resistant nature of zirconia puts the restriction on this method.[36] ND35R8HCL shows crystallite size of 25.8 nm along with a smaller fraction of particles with crystallite size 18.7 nm. While ND35OXDHCL shows crystallite size of range 27.4 nm along with a fraction of particles of crystallite size 18.8 nm.

Fig. 3(a) shows Raman spectra of ND0, ND9, ND20 and ND35 (initial, 09 hours, 20 hours and 35 hours milled) samples. These spectra were fitted with Lorentzian line shapes with slanted linear background to monitor the change in spectral parameter with milling time and on purification as shown in Fig. 3(b) for ND0. Changes in the spectral parameters are summarized in Table SII.† Raman spectra show two prominent features in the range 1300–1400 $cm^{-1}$ and 1500–1600 $cm^{-1}$ known as D and G modes of carbon. D-mode of the sample consists of two Lorentzian components namely 1331.8 and 1351.5 $cm^{-1}$ with FWHM of 5.9 and 62.3 respectively. Peak at 1331.8 $cm^{-1}$ is assigned to triply degenerate ($F_{2g}$) zone center phonon mode of diamond lattice (arising from $O_h^7$ space group),[37] while peak at 1351.5 $cm^{-1}$ with relatively larger peak width is assigned to dis-ordered $sp^3$ bonded carbon structure/amorphous carbon.[38] Peak at 1351.5 $cm^{-1}$ arises from lattice distortion induced breakdown of momentum conservation requirement, which activates phonons at the interior *K* point

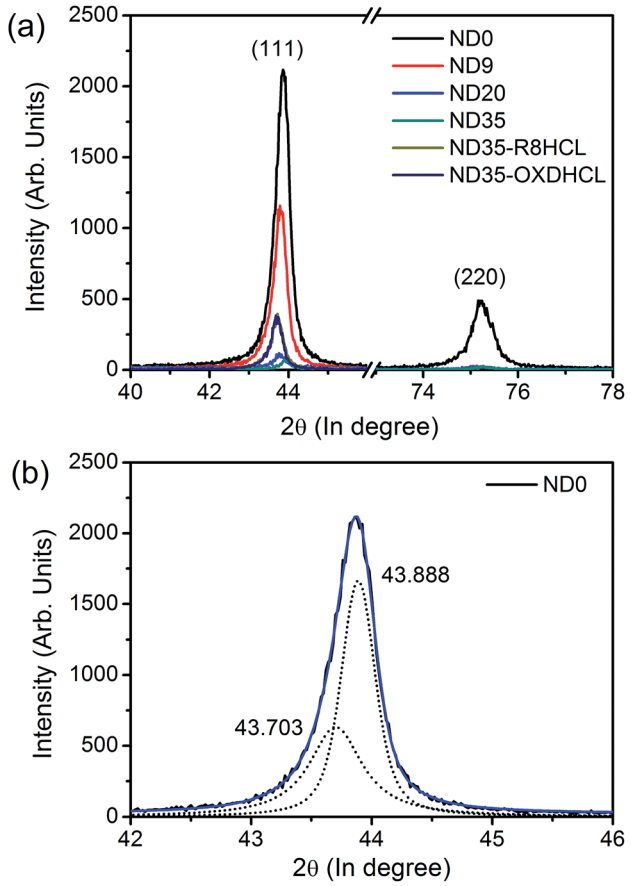


Fig. 2 (a) Shows XRD pattern of the diamond particles milled for 0 hours (ND0), 9 hours (ND9), 20 hours (ND20) and 35 hours (ND35) and purified NDs ND35-R8HCL and ND35-OXDHCL. (b) Fitted (111) peak of ND0 using two Voigt components.

of the Brillouin zone ($q \neq 0$).[39] In addition to D-modes, spectra show peaks at 1482.3 $cm^{-1}$, 1578.7 $cm^{-1}$, 1615.7 $cm^{-1}$ and 1688.2 $cm^{-1}$. Peak at ~1578.8 $cm^{-1}$ is assigned to the graphitic G-mode of carbon arising from intra layer doubly degenerate $E_{2g}$ mode of $sp^2$ bonded graphitic carbon structure, while peak at 1615.7 $cm^{-1}$ is assigned to defect related D′-mode of carbon.[40] D′-band arises due to breakdown of $q = 0$ wave vector selection rule and has been observed for graphite samples with crystallite sizes less than 10 nm.[41] In few samples, we observed peaks at ~1480 $cm^{-1}$ *i.e.* in between D and G modes. Origin of this peak has been assigned to polyacetylene and has nothing to do with C–C $sp^3$ carbon.[42,43] The peak position of $F_{2g}$ mode changes from 1331.8 $cm^{-1}$ to 1330.8 $cm^{-1}$, 1332.5 $cm^{-1}$, 1331.5 $cm^{-1}$ after 9 hours, 20 hours and 35 hours of milling. The back and forth oscillating Raman peak position of $F_{2g}$ mode arises from the compressive and elongation strain produced upon milling.[44] The observed fluctuations in the peak position about 1331.8 $cm^{-1}$ is in agreement with XRD measurements which show oscillatory shifts in the $2\theta$ position with milling time. Analogous to the D-band, G-band also shows variation in the peak position with milling time. Peak observed at 1578.7 $cm^{-1}$ shifts to 1583.4 $cm^{-1}$, 1584.4 $cm^{-1}$ and 1586.8 $cm^{-1}$ upon 09 hours, 20 hours and 35 hours of milling. Further the FWHM of G peak monotonically decreases with increasing milling time indicating increasing graphitic ordering with milling impacts on diamond particles. It is in agreement with the particle size measurements which show the agglomeration of the particles.

Fig. 3(c) shows the Raman spectra of as procured, milled and purified samples from the two different methods. The estimated relative content of the $sp^2$ and $sp^3$ hybridized carbon content is estimated from the area under D and G modes in the Raman spectra. Initial sample ND0 contains 66.4 wt% of $sp^2$ carbon, 12.4 wt% of $sp^3$ diamond structure and 21.2 wt% of disordered $sp^3$ carbon. Post milling the sample purified through acid reflux contains 27.3 wt% of diamond $sp^3$ phase, 30.6 wt% of disordered $sp^3$ structure and 42.1 wt% of $sp^2$ carbon. Air oxidized sample contains 57.4 wt% of $sp^3$ hybridized carbon, 23.2 wt% of disordered carbon and just 19.4 wt% of $sp^2$ carbon. Purification by air oxidation appears to be better method for removal of $sp^2$ carbon impurities from Raman spectroscopy measurements. In addition to it, amount of disordered carbon structure is also relatively less in case of purification by air oxidation. Fig. 3(d) shows the comparative Raman spectra of initial and purified samples before irradiation (ND0, ND35-R8HCL and ND35-OXDHCL) and after irradiation ND0-IRR, ND35-R8HCLIRR and ND35-OXDHCLIRR. ND0-IRR shows decrease in the $sp^3$ wt% content from 12.4 wt% to 0.4 wt% of diamond content. The acid refluxed and ion-irradiated sample (ND35-R8HCLIRR) shows decrease in the diamond content from 27.4 wt% to 0.5 wt%, while air oxidized and ion-irradiated sample (ND35-OXDHCLIRR) shows decrease in the diamond content from 57.4 wt% to 12.5 wt%. Ion-irradiation leads to significant amount of $sp^3$ to $sp^2$ conversion. Additionally, the amount of disordered $sp^3$ carbon content (30.6 wt%) is higher in sample purified through acid reflux as compared to air oxidized sample (23.2 wt%). Interestingly, the sample purified through air oxidation is more resistant to $He^+$-ion irradiation for creating NV centers.

Fig. 4 shows the X-ray photoelectron spectra (XPS) of ND0, ND35, ND35-R8HCL and ND35-OXDHCL. Fig. 4(a), the survey spectra of these samples show peaks at binding energies at 285.1, 399.2 and 531.3 eV corresponding to C 1s, N 1s, O 1s cores respectively. Fig. 4(b) shows C 1s core spectra. Fig. 4(c) shows the typical fitting to the C 1s core level spectra of the ND0 using XPSPEAK 4.1. Similarly, N 1s and O 1s core level was fitted. The summary of the fitted peak profile for all the samples are summarized in Table-SIII and SIV (ESI†) for C 1s core and in Table-SV (ESI†) for N 1s and O 1s cores. Inset of the Fig. 4(c) shows presence of peak at 400.1 eV for initial sample ND0 indicating presence of nitrogen dopants in diamond lattice. Fig. 4(d) shows the O 1s core spectra. The atomic concentrations of carbon, oxygen and nitrogen were estimated using corresponding peak area after background subtraction normalized to the inelastic mean free path, photoionization cross-section ($\sigma$) and analyzer transmission function ($2^{nd}$ order approximation). The photoionization cross-section ($\sigma$) was taken as 0.013 for C 1s core, 0.040 for O 1s core and 0.024 for N 1s core. Inelastic mean free path (IMFP) was taken as 33.03 Å, 26.53 Å and 29.51 Å for C 1s core, O 1s core and N 1s core respectively. The

 

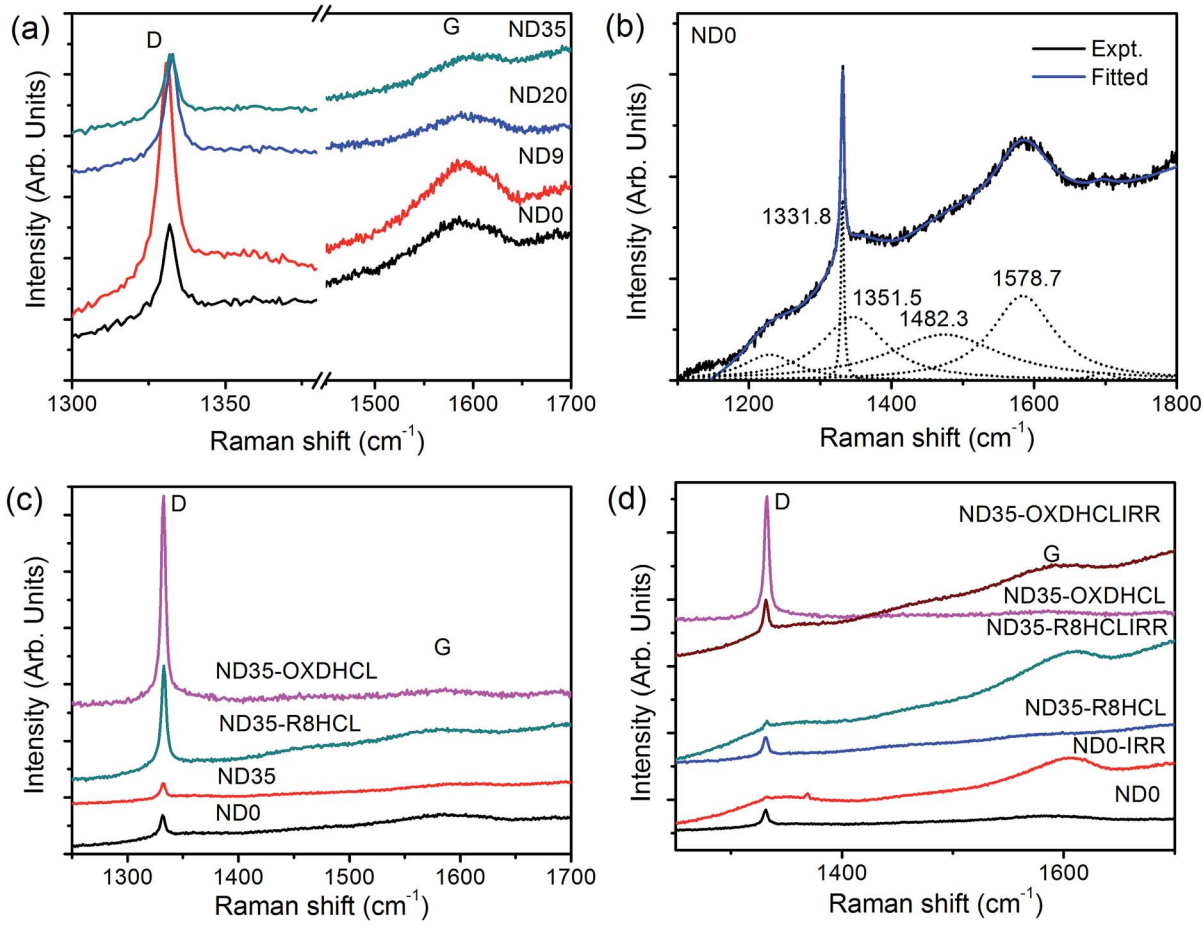


Fig. 3 (a) Raman spectra of diamond milled for different duration. (b) Fitted spectral line profile of ND0 using Lorentzian line shapes with slanted linear background. (c) Raman spectra of ND0, ND35, ND35-R8HCL and ND35-OXDHCL. (d) Raman spectra of ND0, ND35, ND35-R8HCL and ND35-OXDHCL before and after irradiation. Sharp D-band component (FWHM $\sim$ 6 $cm^{-1}$) represents diamond content, broad D-band represents disordered $sp^3$ carbon and G-band represents graphitic carbon.

compositions of different samples obtained from this procedure are listed in Table-SVI (ESI†).

ND0 shows peaks of nitrogen and oxygen in addition to carbon core, Fig. 4(a). C 1s core spectra of ND0 exhibits peak at 286.2 eV and 286.9 eV, corresponding to $sp^2$ and $sp^3$ hybridized carbon. These peaks are shifted towards high binding energy as compared to expected 284.3 eV and 285.2 eV peak from $sp^2$ and $sp^3$ carbon respectively.[45,46] The initial sample is estimated to contain 79.9 wt% of $sp^2$ carbon and 20.0% of $sp^3$ carbon. This is in close agreement with estimated $sp^2$ (66.4%), $sp^3$ carbon (12.4%) and disordered $sp^3$ carbon (21.1%) from Raman spectroscopy. Since X-rays have finite penetration depth ($\sim$4 nm), XPS studies are more sensitive to surface stoichiometry and it shows that the outer surface of the particles contains higher graphitic carbon. The $sp^2$ hybridized carbon and outer surface atoms terminated with oxygen containing functional groups (as evidenced from observation of O 1s core) stabilizes the nanoparticles by terminating dangling bonds. Two plasmon loss peaks are also observed at 313.0 eV and 321.0 eV with an unidentified peak at 340.1 eV. Shift in the $sp^2$ and $sp^3$ bonded carbon peaks against the reference binding energy for these two cores is mainly due to defects and small primary particle size. Defects are present at the surface due to the abrupt discontinuity of the diamond phase and leads to the disturbance of charge neutrality. The band bending increases the binding energy of C 1s spectra.[47] In addition to band bending, it may have contribution from charging effects due to insulating diamond nanoparticles.[48] ND35 shows peaks at slightly lower binding energy at 285.2 eV and 285.7 eV for $sp^2$ and $sp^3$ hybridized carbon amounting to 80.2 wt% and 19.8 wt% respectively. In case of ND35, plasmon loss peaks are also observed at smaller binding energies (309.0 eV and 319.5 eV) supporting the understanding that in case of milled sample presence of metallic impurities reduces the charging effects. Change in the binding energy for the carbon core reveals that iron contamination leads to the agglomeration of primary particles along with abrupt reduction in the surface defects and reduction in the band bending contribution. This is in agreement with agglomeration observed in the particle size analysis (Fig. S2(d); ESI†).

The sample purified through acid reflux ND35-R8HCL shows oxidized surface features with the reduced $sp^2$ carbon near the

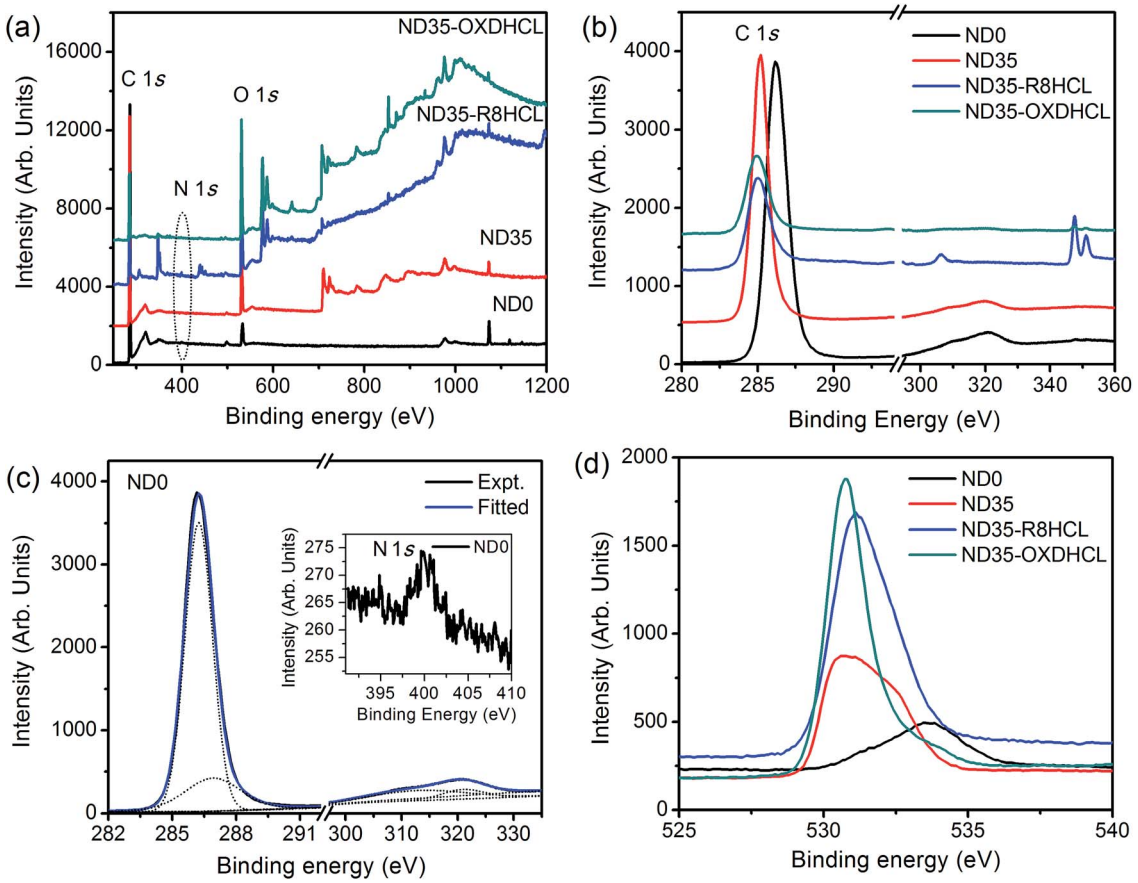


Fig. 4 Shows XPS spectra. (a) Shows the survey scan spectra of ND0, ND35, ND35-R8HCL and ND35-OXDHCL. (b) Shows the C 1s carbon core peak. (c) Fitting of C 1s core peak, typically shown for ND0. Inset shows peak observed in the range 395–410 eV corresponding to N 1s core. (d) Shows O 1s core-spectra.

surface. In case of ND35-R8HCL, the binding energies of $sp^2$ (285.0 eV) and $sp^3$ (286.2 eV) hybridized carbon atoms are lower than the initial ND0. Chemical etching of graphitic and amorphous carbon layers results into observed lower binding energy. ND35-R8HCL contains 26.1 wt% $sp^2$ carbon and 17.3 wt% $sp^3$ carbon. Presence of different oxygen containing groups is confirmed by presence of peaks at 288.8 eV, 294.4 eV, and 297.0 eV (corresponding to C–O, C═O and O═C–O species).[49] Functionalized carbon atoms amount to 56.6 wt% of the sample. Reduction of the graphitic layers is in agreement with observations in Raman spectra where the G band is diminished in the acid refluxed sample. Reduction of the graphitic layers and subsequent de-agglomeration due to the presence of the oxygen containing groups is also confirmed by dynamic light scattering based particle size analysis measurements for acid refluxed sample. Also, a weak plasmon loss peak is observed at 306.3 eV. On the other hand, ND35-OXYHCL contains 77.3 wt% $sp^2$ carbon (284.9 eV) and 14.2 wt% $sp^3$ carbon (286.5 eV). In addition, it contains two peaks at 291.1 eV and 293.7 eV showing presence of oxygen containing groups amounting to 8.5 wt% of the sample. Plasmon loss peaks are observed at 307.6 eV and 318.9 eV.

Irradiated sample ND0-IRR contains 64.3 wt% $sp^2$ and 35.7 wt% $sp^3$ carbon with peaks at 285.3 eV and 286.5 eV respectively. Irradiation and subsequent annealing result into modification of outer surface and leads to reduction of $sp^2$ carbon on the surface. $sp^2$ and $sp^3$ peaks were found to shift towards lower binding energy as compared to ND0 possibly due to the surface defect reduction on annealing. Irradiation of the acid refluxed sample (ND35-R8HCLIRR) leads to more graphitization on the outer core and the oxygen related functional groups are detached from the outer surface. In case of ND35-R8HCLIRR, the $sp^2$ carbon (285.4 eV) is found to account for 72.4 wt%, $sp^3$ carbon for 23.1 wt% (285.9 eV peak) and functionalized carbon atoms amounts to 4.4 wt%. Peak at 293.7 eV shows the presence of functional oxygen groups at the outer surface, survived by irradiation and annealing. While, ND35-OXDHCLIRR is found to contain 16.7 and 5.6 wt% of $sp^2$ and $sp^3$ carbon respectively along with 77.6 wt% fraction of functionalized carbon atoms. In case of ND35-OXDHCLIRR, the $sp^2$ and $sp^3$ peaks are observed towards higher binding energy side at 288.7 and 288.9 eV respectively. Even the plasmon loss peaks are observed towards higher binding energy side at 314.0 eV and 324.8 eV.

Analysis of the N 1s core (Table SV; ESI†) of ND0 shows peak at 400.1 eV. It indicates presence of nitrogen. N 1s core peak was not observed for ND35 within sensitivity limit of XPS, probably due to lattice relaxation and surface reconstruction during

 

milling. Structural reconstructions lead to nitrogen migration towards the center of the primary particles. N 1s core peak was not observed in all other samples, except ND35-OXDHClIRR. The understanding about presence of substitutional nitrogen atoms on the surface within X-ray penetration depth only for ND35-OXDHCLIRR is not clear to us. Fig. 4(d) shows the O 1s core spectra. Calculated peak area of O 1s core reveals that more oxygen is incorporated on the diamond particles during milling. Further, the amount of oxygen attached to the particle surfaces increases during purification. ND0 shows the presence of carbon oxygen double bond species (C=O) (531.4 eV), nitrosyl (533.6 eV), and hydro peroxide groups (536.3 eV) (Table SV; ESI†).[50] ND35 shows the presence of nitrosyl (532.2 eV), alcoholic (530.2 eV) and carbon oxygen double bond (C=O) species (530.8 eV). ND35-R8HCL also reveals the presence of carbon oxygen double bond (C=O) species (531 eV) and nitrosyl (532.5 eV) with large surface areas, *i.e.* surface is dominated by the oxygen containing groups. In case of ND35-OXYHCL in addition to carbon oxygen double bond (C=O) species and nitrosyl groups (533.8 eV); a prominent peak is also appears at 530.7 eV. Interestingly, ND35-R8HCL contains more surface functionalized oxygen than the ND35-OXDHCL.

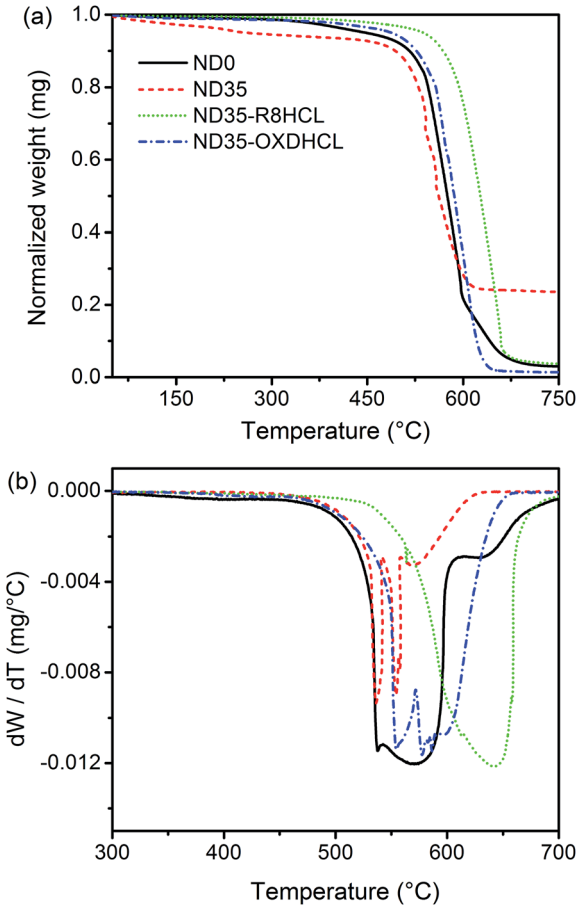


Fig. 5 (a) TGA pattern of ND0, ND35, ND35-R8HCL and ND35-OXDHCL. The corresponding DTA pattern is shown in (b). The sample purified through acid reflux shows relatively higher thermal stability than the sample purified through air oxidation.

Fig. 5(a) shows the Thermo-gravimetric analysis (TGA) pattern. ND0 and ND35 shows similar oxidation pattern although the amount of residue left after oxidation differs significantly. The ND0 shows nearly complete oxidation with only 3.1 wt% as residue, while ND35 shows about 23.8% residue leftover after oxidation, probably from iron particles incorporated from balls and vials used for milling. ND35-R8HCL shows higher oxidative stability with steeper oxidation. The differential thermo-gravimetric analysis (DTA) curve of ND0 shows three peak structure with corresponding maxima in the oxidation at 397 °C, 537 °C, 571 °C and 631 °C amounting to oxidation of 3.3 wt%, 12.4 wt%, 29.8 wt% and 41.5 wt% sample respectively indicating presence of four different phases of carbon, Fig. 5(b). The milled sample ND35 also shows four different components at 536 °C, 554 °C, 558 °C and 569 °C accounting for the 22.8 wt%, 16.7 wt%, 8.9 wt% and 6.5 wt% of the sample respectively. In contrast to the initial and milled samples, the purified sample ND35-R8HCL shows only one maxima in the DTA curve at 642 °C, while in case ND35-OXDHCL three maxima were observed in the DTA curve at 554 °C, 577 °C and 596 °C representing 18.7, 20.7 and 21.3% weight loss. In case of sample purified through wet chemical route 3.4 wt% metallic residue was left, while in case of sample purified through air oxidation 1.3 wt% of the residue was observed.

Fig. 6(a) shows the fluorescence (FL) spectra. FL spectra were fitted with Gaussian line shape, typically shown for ND35-R8HCLIRR in Fig. 6(b). The fitted spectral line profile parameters are listed in Table SVII (ESI†). ND0 shows very weak and broad emission intensity. Emission intensity of milled sample ND35 is further suppressed extensively due to incorporation of iron particles, a well-known fluorescence quencher.[51] On purification, ND35-R8HCL and ND35-OXDHCL shows emission intensity similar to ND0. In addition, two weak peaks are seen sitting on the broad background on close observation at 552 and 559 nm. These are D and G Raman modes. Except ND35-OXDHCL sample, characteristics emission of NV center is not observed in non-irradiated samples. ND35-OXDHCL shows weak characteristic zero phonon line (ZPL) for $NV^{\circ}$ (575 nm) and $NV^{-}$ centers (638 nm). It is due to relatively efficient iron contamination removal by air oxidation method, which is also confirmed from TGA measurements. The emission intensity was multifold enhanced with creation of NV centers in NDs by ion irradiation. ND0-IRR shows broad FL with Gaussian components at 605, 655 and 695 nm along with a sharp feature at 576 nm. The sharp peak is band-edge transition of $NV^{\circ}$ centers.[52] ND0-IRR sample shows broad emission peaks of the sidebands of $NV^{\circ}$ and $NV^{-}$ but zero phonon line (ZPL) of these color centers are unresolvable. The emission intensity of ND0-IRR for side bands and ZPL is weaker as compared to ND35-R8HCLIRR and ND35-OXDHCLIRR samples. It is due to the exciton trapping at outer $sp^2$ surface layers of ND0-IRR which are diminished after oxidation. ND35-R8HCLIRR shows two prominent sharp peaks at 575 nm ($NV^{\circ}$) and 638 nm ($NV^{-}$) sitting over broad intense FL in the range 525–750 nm. Broad emission can be resolved into four Gaussian components at 605 nm, 658 nm, 660 nm and 698 nm respectively. These components are the vibronic side band emission owing to the

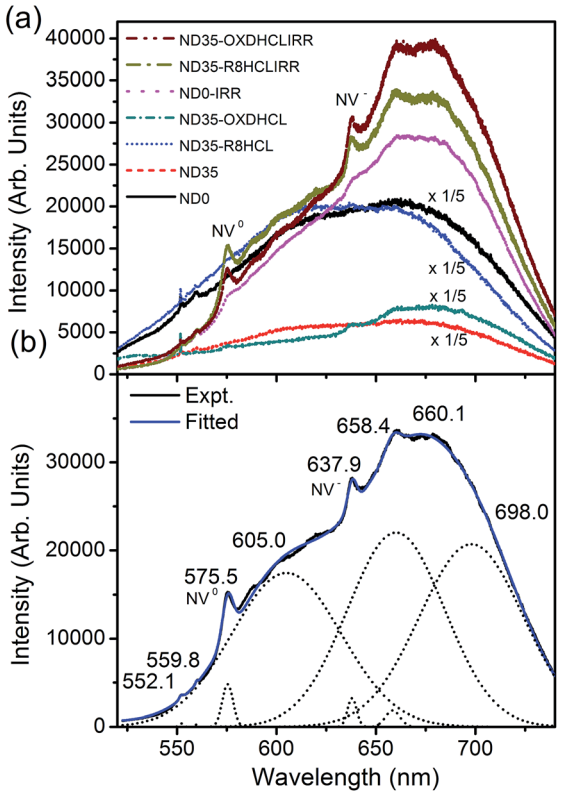


Fig. 6 (a) Shows fluorescence spectra of NDs before irradiation (ND0, ND35, ND35-R8HCL, ND35-OXDHCL) and after irradiation (ND0-IRR, ND35-R8HCLIRR, ND35-OXDHCLIRR). The intensity of curves for NDs before irradiation (ND0, ND35, ND35-R8HCL, ND35-OXDHCL) have been scaled up by a factor of 5 for clear visualization. (b) FL spectra were fitted using Gaussian components, typically shown for ND35-R8HCLIRR. It shows characteristic emission peak at 575.5 and 637.9 nm of $NV^{\circ}$ and $NV^{-}$ defect centers along with broad vibronic side band emission extended up to 750 nm.

electron–phonon interaction at room temperature. Similarly, ND35-OXDHCLIRR shows sharp emission peaks at 575.1 nm ($NV^{\circ}$) and 637.8 nm ($NV^{-}$) along with broad emission peaks. The broad emission peak of ND35-OXDHCLIRR can also be resolved into four Gaussian components centered at 600.8, 658.6, 675.6 and 715.8 nm (vibronic side bands). Fitted spectral parameters show that the emission intensity due to $NV^{-}$ centers is much stronger than the emission intensity due to $NV^{\circ}$ centers in ND35-OXDHCLIRR. This is in contrast to the ND35-R8HCLIRR where $NV^{\circ}$ centers shows the more intense ZPL intensity than $NV^{-}$. The ND35-OXDHCLIRR NDs shows stronger emission in the red region than the ND35-R8HCLIRR NDs.

## Conclusions

We have shown that the fluorescence from NV center engineered NDs depends upon the oxidation methods. We observed that the diamond particles can be de-agglomerated into smaller particles upon ball milling, while crystallite size does not change. Sample purified through acid reflux shows smaller size NDs than the air oxidized ones. Acid refluxed NDs were more water dispersible than the air oxidized samples. Acid refluxed NDs were primarily rectangular in shapes while air oxidized NDs contained equal mixture of rectangular and irregular shaped particles. Purification by air oxidation was observed to be more efficient for $sp^2$ carbon removal from Raman spectroscopy and contained less defects. While on the outer surface, particles contained higher density of $sp^2$ carbon in case of air oxidized samples as revealed through XPS. Sample purified through air oxidation shows relatively intense fluorescence than purified through acid reflux. Since for bio-imaging applications water dispersible NDs with defined shape are desirable with sufficient FL intensity, purification by acid reflux should be preferred for such uses. While for nano-photonic applications, where the irregularity of diamond particle shape is not a real concern; purification by air oxidation is recommended which gives intense FL intensity. Thus depending upon the end use of NDs, whether it is bio-photonics or nano-photonics, we need to follow purification by acid reflux and air oxidation respectively.

## Acknowledgements

Dilip K. Singh thanks DST, Govt. of India for financial support through Inspire faculty award (IFA-13 PH-65).

## References

1 P. Pantazis, J. Maloney, D. Wu and S. E. Fraser, *Proc. Natl. Acad. Sci. U. S. A.*, 2010, **107**, 14535–14540.
2 E. Rittweger, K. Y. Han, S. E. Irvine, C. Eggeling and S. W. Hell, *Nat. Photonics*, 2009, **3**, 144–147.
3 K. I. Willig, B. Harke, R. Medda and S. W. Hell, *Nat. Methods*, 2007, **4**, 915–918.
4 M. J. Rust, M. Bates and X. Zhuang, *Nat. Methods*, 2006, **3**, 793–796.
5 P. Annibale, S. Vanni, M. Scarselli, U. Rothlisberger and A. Radenovic, *PLoS One*, 2011, **6**, e22678.
6 Y. Zhu, J. Li, W. Li, Y. Zhang, X. Yang, N. Y. Sun, Y. Zhao, C. Fan and Q. Huang, *Theranostics*, 2012, **2**, 302.
7 S. Yu, M. Kang, H. Chang, K. Chen and Y. Yu, *J. Am. Chem. Soc.*, 2005, **127**, 17604–17605.
8 A. gruber, A. Dräbenstedt, C. Tietz, L. fleury, J. wrachtrup and C. von borczyskowski, *Science*, 1997, **276**, 2012–2014.
9 F. Jelezko, C. Tietz, A. Gruber, I. Popa, A. Nizovtsev, S. Kilin and J. Wrachtrup, *Single Mol.*, 2001, **2**, 255–260.
10 F. Jelezko and J. Wrachtrup, *Phys. Status Solidi A*, 2006, **203**, 3207.
11 Y. Chen, H. Shu, Y. Kuo, Y. Tzeng and H. Chang, *Diamond Relat. Mater.*, 2011, **20**, 803–807.
12 J. Boudou, P. Curmi, F. Jelezko, J. Wrachtrup, P. Aubert, M. Sennour, G. Balasubramanian, R. Reuter, A. Thorel and E. Gaffet, *Nanotechnology*, 2009, **20**, 235602.
13 V. N. Mochalin, O. Shenderova, D. Ho and Y. Gogotsi, *Nat. Nanotechnol.*, 2012, **7**, 11–23.
14 V. Y. Dolmatov, *Russ. Chem. Rev.*, 2001, **70**, 607.
15 G. Yang, J. Wang and Q. Liu, *J. Phys.: Condens. Matter*, 1998, **10**, 7923.

 

16 A. Stacey, I. Aharonovich, S. Prawer and J. E. Butler, *Diamond Relat. Mater.*, 2009, **18**, 51–55.
17 C. Kittel, *Introduction to Solid State Physics*, 8th edition, 2012.
18 S. Osswald, G. Yushin, V. Mochalin, S. O. Kucheyev and Y. Gogotsi, *J. Am. Chem. Soc.*, 2006, **128**, 11635–11642.
19 L. L. Huang and H. Chang, *Langmuir*, 2004, **20**, 5879–5884.
20 S. Stehlik, M. Varga, M. Ledinsky, V. Jirasek, A. Artemenko, H. Kozak, L. Ondic, V. Skakalova, G. Argentero, T. Pennycook, J. C. Meyer, A. Fejfar, A. Kromka and B. Rezek, *J. Phys. Chem. C*, 2015, **119**, 27708–27720.
21 C. A. Schneider, W. S. Rasband and K. W Eliceiri, *Nat. Methods*, 2012, **9**, 671–675.
22 P. K. Giri, S. Bhattacharyya, D. K. Singh, R. Kesavamoorthy, B. K. Panigrahi and K. G. M. Nair, *J. Appl. Phys.*, 2007, **102**, 093515.
23 A. Pentecost, S. Gour, V. Mochalin, I. Knoke and Y. Gogotsi, *ACS Appl. Mater. Interfaces*, 2010, **2**, 3289–3294.
24 N. Wada and S. A. Solin, *Physica B+C*, 1981, **105**, 353–356.
25 A. C. Ferrari and J. Robertson, *Philos. Trans. R. Soc., B*, 2004, **362**, 2477.
26 A. Jorio, R. Saito, G. Dresselhaus and M. S. Dresselhaus, *Raman spectroscopy in Graphene related systems*, Wiley VCH 2010.
27 D. K. Singh, P. K. Iyer and P. K. Giri, *J. Appl. Phys.*, 2012, **111**, 064304.
28 Y. Kawashima and G. Katagiri, *Phys. Rev. B: Condens. Matter Mater. Phys.*, 1995, **52**, 10053.
29 A. C. Ferrari and J. Robertson, *Phys. Rev. B: Condens. Matter Mater. Phys.*, 2001, **63**, 121405.
30 A. C. Ferrari and J. Robertson, *Philos. Trans. R. Soc., A*, 2004, **362**, 2269–2270.
31 D. K. Singh, P. K. Iyer and P. K. Giri, *Diamond Relat. Mater.*, 2010, **19**, 1281.
32 F. Y. Xie, W. G. Xie, J. Chen, X. Liu, D. Y. Lu and W. H. Zhang, *J. Vac. Sci. Technol., B*, 2008, **26**, 102–105.
33 M. J. Webb, P. Palmgren, P. Pal, O. Karis and H. Grennberg, *Carbon*, 2011, **49**, 3242–3249.
34 I. Kusunoki, M. Sakai, Y. Igari, S. Ishidzuka, T. Takami, T. Takaoka, M. nishiani- Gamo and T. ando, *Surf. Sci.*, 2001, **492**, 315–328.
35 Y. Fan, A. G. Fizgerald, P. John, C. E. Troupe and J. I. B. Wilson, *Surf. Interface Anal.*, 2002, **34**, 703–707.
36 H. Estrade-Szwarckopf, *Carbon*, 2004, **42**, 1713–1721.
37 G. Cunningham, A. M. Panich, A. I. Shames, I. Petrov and O. shenderova, *Diamond Relat. Mater.*, 2008, **17**, 650–654.
38 B. Bodenant, F. Fages and M. Delville, *J. Am. Chem. Soc.*, 1998, **120**, 7511–7519.
39 I. Aharonovich, S. Castelletto, D. A. Simpson, C. Su, A. D. Greentree and S. Prawer, *Rep. Prog. Phys.*, 2011, **74**, 076501.
40 D. K. Singh, P. K. Iyer and P. K. Giri, *J. Appl. Phys.*, 2012, **111**, 064304.
41 Y. Kawashima and G. Katagiri, *Phys. Rev. B: Condens. Matter Mater. Phys.*, 1995, **52**, 10053.
42 A. C. Ferrari and J. Robertson, *Phys. Rev. B: Condens. Matter Mater. Phys.*, 2001, **63**, 121405.
43 A. C. Ferrari and J. Robertson, *Philos. Trans. R. Soc. London, Ser. A*, 2004, **362**, 2269–2270.
44 D. K. Singh, P. K. Iyer and P. K. Giri, *Diamond Relat. Mater.*, 2010, **19**, 1281.
45 F. Y. Xie, W. G. Xie, J. Chen, X. Liu, D. Y. Lu and W. H. Zhang, *J. Vac. Sci. Technol., B: Microelectron. Nanometer Struct.–Process., Meas., Phenom.*, 2008, **26**, 102–105.
46 M. J. Webb, P. Palmgren, P. Pal, O. Karis and H. Grennberg, *Carbon*, 2011, **49**, 3242–3249.
47 I. Kusunoki, M. Sakai, Y. Igari, S. Ishidzuka, T. Takami, T. Takaoka, M. Nishiani-Gamo and T. Ando, *Surf. Sci.*, 2001, **492**, 315–328.
48 Y. Fan, A. G. Fizgerald, P. John, C. E. Troupe and J. I. B. Wilson, *Surf. Interface Anal.*, 2002, **34**, 703–707.
49 H. Estrade-Szwarckopf, *Carbon*, 2004, **42**, 1713–1721.
50 G. Cunningham, A. M. Panich, A. I. Shames, I. Petrov and O. Shenderova, *Diamond Relat. Mater.*, 2008, **17**, 650–654.
51 B. Bodenant, F. Fages and M. Delville, *J. Am. Chem. Soc.*, 1998, **120**, 7511–7519.
52 I. Aharonovich, S. Castelletto, D. A. Simpson, C. Su, A. D. Greentree and S. Prawer, *Rep. Prog. Phys.*, 2011, **74**, 076501.